



## Study of vapor film dynamics and heat transfer through an image processing technique



Faith R. Beck<sup>\*</sup>, Nurali Virani<sup>1</sup>, Lokanath Mohanta<sup>2</sup>, Faruk A. Sohag<sup>3</sup>, Asok Ray, Fan-Bill Cheung

Department of Mechanical and Nuclear Engineering, The Pennsylvania State University, University Park, PA 16802, United States

### ARTICLE INFO

#### Article history:

Received 7 February 2018

Received in revised form 17 April 2018

Accepted 18 April 2018

#### Keywords:

Film boiling

Image processing

Downward-facing boiling

Interfacial oscillations

Interfacial heat transfer coefficient

Interfacial heat flux

### ABSTRACT

Understanding of two-phase heat transfer mechanisms on downward-facing hemispherical vessels is crucial during external reactor vessel cooling (ERVC) under severe accident conditions. Film boiling is the predominant heat transfer regime in the initial stages of quenching under these circumstances. In this work, the process of downward-facing film boiling on the outer surface of a hemispherical vessel is studied using high-speed video. High-speed video is a valuable measurement technique because it does not require any invasive sensors that may alter the natural liquid-vapor interface in film boiling. With high-speed video and a few image processing techniques, accurate measurements of film thickness have been made at four different degrees of subcooling (0, 3, 5, and 10 °C) and angular locations (0, 14, 28, and 42°) on a hemispherical vessel. With increasing subcooling and decreasing angular location, the vapor film thickness has been found to decrease. Average film thickness at 0 °C (respectively, 10 °C) subcooling and one second after immersion is found to be approximately 2 mm (respectively, 0.5 mm). High-speed videos taken at 650 frames per second (fps) have shown significant oscillations at the liquid-vapor interface during film boiling. Additionally, oscillations in the film thickness and its wave characteristics have been analyzed at the prescribed angular locations and degrees of subcooling. From the visual data, insights regarding the heat transfer behavior of film boiling are obtained. Additionally, the characteristics of the interfacial oscillations have been related to the heat flux distribution. The mechanism for the interfacial oscillations can be attributed to disturbances in the balance between the wall and interfacial heat fluxes, along with the hydrodynamic instability.

© 2018 Elsevier Ltd. All rights reserved.

### 1. Introduction

A properly designed nuclear power plant can provide safe and consistent energy under well-controlled operating conditions; nevertheless, radiation protection is still a large concern. Currently there are multiple layers of protection for the safekeeping of radioactive materials such as a containment layer, holding of fission gases by the fuel pellets themselves, and cladding around the fuel rods. All of these layers are housed inside the reactor pressure vessel (RPV), which is retained in a containment building. During a severe accident, fuel pellets rupture and the fuel rod cladding melts, which can cause a meltdown of the reactor core, with molten corium relocating downward into the bottom head of the

RPV. Therefore, during such accidents, it is crucial to maintain the integrity of the RPV lower head for in-vessel retention (IVR) of the molten corium to achieve in-vessel cooling; this effort minimizes the risk of containment failure. In order to contain the radioactive molten corium within the reactor, the reactor cavity is flooded with coolant to submerge the entire RPV. This method, also known as IVR through external reactor vessel cooling (ERVC), allows for the removal of decay heat from the molten corium through the vessel wall by downward-facing boiling (DFB) on the vessel outer surface.

In spite of its practical importance, most of the research related to DFB has been conducted only in the past 20 years. Of the DFB experiments performed, it has been found that there is a significant spatial variation of the critical heat flux (CHF) with angular location [1,2]. The cyclic nature of the vapor dynamics and the resulting two-phase motion along the heated surface for DFB have been observed visually. It was found that the vapor departure velocity and the CHF changed with the angle of orientation of the heated surface [3]. Furthermore, the net rate of vapor generation reduced significantly with the increase in bulk liquid subcooling, such that the bubble residence times at the CHF were independent of the

<sup>\*</sup> Corresponding author.

E-mail address: [frb115@psu.edu](mailto:frb115@psu.edu) (F.R. Beck).

<sup>1</sup> Current address: General Electric Global Research, Niskayuna, NY 12309, United States.

<sup>2</sup> Current address: United Technologies Corporation, Syracuse, NY 13221, United States.

<sup>3</sup> Current address: Ford Motor Company, Allen Park, MI 48101, United States.

subcooling [4]. Additionally, Cheung et al. [5–8] observed significant spatial variation of the CHF, with its local limit increasing monotonically from the bottom center to the equator of the vessel for both saturated and subcooled boiling. Sohag et al. [9–11] and Segall et al. [12], investigated the effects of subcooling and micro-porous coatings on the enhancement of DFB on a hemispherical vessel. They also found that the CHF is dependent on the angular locations and surface conditions for these types of geometries. In the present work, the effects of subcooling on the vapor film thickness, interfacial vapor velocity, and interfacial wave frequency for a downward-facing hemisphere have been determined quantitatively. These measurements were made using an image processing technique involving high-speed video to determine the vapor film thickness as a function of submersion time and angular location.

Utilizing image processing techniques, which capture the physics of two-phase flows without the need for invasive sensors, is a relatively new methodology. Pham et al. [13] studied the interfacial wavy behavior of two-phase flows on a rod bundle geometry via high-speed video in 2014. They later built on this work in 2015 [14] by processing the images they collected to determine mean film thicknesses, wave height, power spectral density (PSD), and wave velocity that were used to characterize the interaction mechanisms along the wavy film. In addition to the work by Pham, other authors have used high-speed video to characterize bubble growth and nucleation processes [15–18]. Besides utilizing imaging to determine two-phase flow dynamics, there has been work to capture the nucleate boiling departure frequency using these methodologies [15,19–26]. Brooks et al. [15] found that bubble departure frequency and size increase with the heat transfer rate. For nucleate boiling frequencies under pool boiling conditions, the following bubble departure frequencies have been observed: 4 Hz for DFB [5], 11 Hz for upward-facing pool boiling [20], 25 Hz for micro-channels [21], and as low as 2 Hz for a Na/Cl pool boiling bath [22]. Depending on the orientation, surface conditions, bath liquid, and applied heat flux, the bubble departure frequency has been found to vary. With this variation, there is a wide selection of models to predict the bubble departure frequency and even size [24]. However, to the best of the authors' knowledge, no literature is available that measures the frequency of the film oscillations, determines a heat transfer coefficient (HTC), or estimates the heat flux in film boiling by making use of high-speed video data.

In this work, a downward-facing hemispherical vessel undergoing quenching is observed using high-speed video. The wall temperature before immersion is well above the minimum film boiling temperature to investigate the effects of liquid subcooling and angular location on film boiling. Some of the characteristics explored in film boiling include: vapor film oscillation frequency with time and vessel temperature; mean, maximum, and minimum film thicknesses; and the relative interfacial vapor film velocity with angular location. In addition to the observed film boiling characteristics, the HTC is computed for a downward-facing hemisphere by making use of the high-speed video data. This determined HTC is compared with results from a published model and found to produce similar results. With the modeled HTC, the heat flux in film boiling is compared using a traditional lumped capacitance method, and a new method that utilizes both the video and thermocouple data.

The remainder of this article is organized as follows: Section 2 describes the experimental setup and approach; Section 3 focuses on the results and discussion; and Section 4 provides the conclusions from this study.

## 2. Experimental setup and approach

The following section focuses on the experimental facility, setup, and approach for acquiring the measured quantities, including the image processing technique and methodology.

### 2.1. Facility

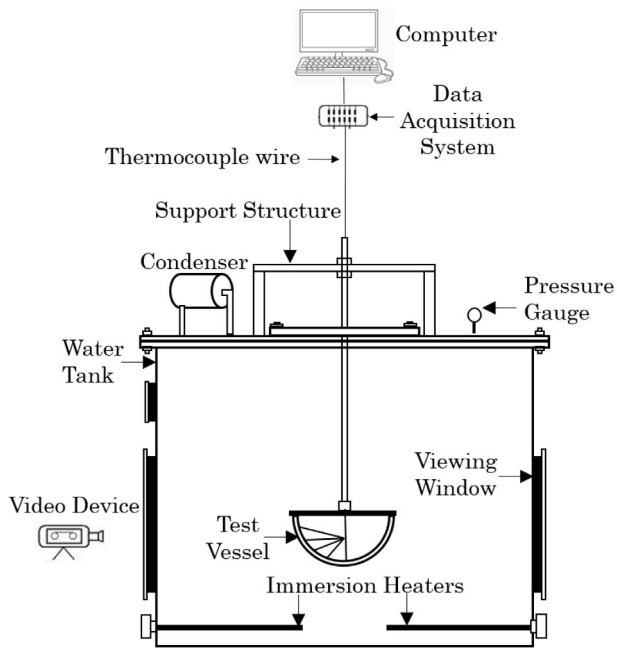
The Subscale Boundary Layer Boiling (SBLB) facility at The Pennsylvania State University is shown in Fig. 1(a). This pool boiling facility contains a cylindrical water tank that is 1.14 m tall and 1.22 m in diameter. The setup simulates a reactor cavity in a nuclear power plant that is sufficiently large to minimize recirculation currents generated due to boiling. Two large viewing windows of diameter 0.558 m are installed on the tank to record the flow as boiling takes place on the outer surface of the test vessel. Three 12 kW immersion heaters around the bottom of the tank are used to preheat the bath to the prescribed temperature. Heating requires between 5 and 6 h before reaching the saturation temperature. During the heat-up process, a temperature gradient is created by natural convection and so three installed thermocouples monitor temperature variation in the tank. While the facility can perform tests at higher pressures, all experiments reported in this study are conducted at atmospheric pressure.

The vessel is made of 304-grade stainless steel, having an outside diameter of 30.48 cm with a wall thickness of 2.54 mm. Four 36-gauge K-type thermocouples are spot welded along an arc starting from bottom center up to the equator of the vessel at 0, 14, 28, and 42° (see Fig. 1(b)). These angular locations were chosen to maximize the number of thermocouples that can be installed on the vessel. The error associated with the temperature measurement is  $\pm 1.1$  °C, or 0.4% of the thermocouple reading within its measurement range. Thermocouple sensors are synchronized with the high-speed video by sampling both signals at the same time instance. In order to negate the radial temperature variation through the vessel wall, 3.81 mm holes with a depth of 1.905 mm are drilled from the inner surface where thermocouples are then spot-welded. Prior to quenching, the vessel is heated to approximately 400 °C and the bath temperature has reached the prescribed subcooling. After preheating, the vessel is manually lowered into the tank via a hollow stainless steel rod, which is connected to the top of the vessel. It takes only a few seconds to lower the vessel into the tank, during which time no significant cooling takes place as the vessel is initially well above the minimum film boiling temperature.

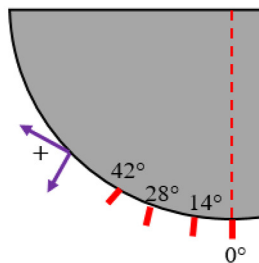
### 2.2. Image processing technique

To capture the film boiling dynamics, high-speed videos are used to measure the instantaneous film thickness at 650 frames per second (fps). Fig. 2 shows a progression of vapor film thickness throughout the quenching process for the 100 °C bath. Notice that the upper angles show larger vapor bubbles than the lower locations in the 15 s frame, suggesting that the upper elevations are in the process of quenching.

To measure the film thickness using high-speed video, the edge of the film must be detected. The color images of the complete quenching process are first converted to binary images by using color thresholding, where the thresholds for each of the three color channels (red, green, and blue) are predetermined. Since the ambient lighting, vessel geometry, and camera were not changed during the experiment, the same settings for image thresholding are used for all experiments. In the binary image, any gaps present along the edges are filled and binary regions having only a few pixels are deleted to filter out any unnecessary noise. Then, edge detection is carried out on the resulting binary image by using a Laplacian of Gaussian filter [27]. An example detected edge is shown in Fig. 3, with both the original and binary images. Once the colored image is converted to a binary edge, a polar-to-Cartesian coordinate transformation is used to obtain the film thickness at each angular location for every instant in time. The location of the center and radius of the vessel are needed for the coordinate



(a) The SBLB pool boiling experimental facility



(b) Vessel orientation with thermocouple locations

Fig. 1. Experimental setup.

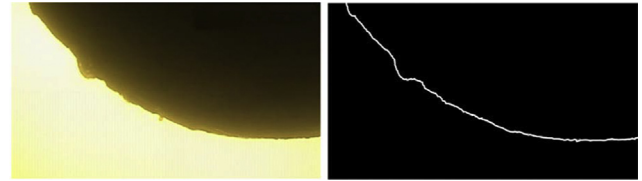


Fig. 3. Original image with processed edge detected for the 97 °C bath.

### 3. Results and discussion

In the following section, the video data is used to study the vapor film interfacial oscillations, thickness with time and temperature, minimum and maximum values at the vessel bottom center, interfacial velocity, interfacial heat transfer coefficient, and heat flux estimation that is compared with a traditional lumped capacitance method.

#### 3.1. Interfacial oscillations

Flow visualization can depict oscillations in the liquid-vapor interface. These oscillations are reflected as a change in the film thickness at a particular angular location displayed in successive high-speed images. The frequencies of the interfacial oscillations at a particular angular location on the vessel wall are analyzed to obtain the dominant frequency. We also examine how this dominant frequency changes with time and subcooling. The bottom 0° angular location is considered in Fig. 4, showing the variation of film thickness with time for the 90 °C bath. Here, a filtered film thickness is overlaid for clarity; the film thickness is filtered with an unbiased, moving average. Note that the point of CHF is denoted on the figure and any time after this point, the 0° location is undergoing nucleate boiling. A 7 Hz (0.14 s) nucleate boiling frequency is determined from Fig. 4.

Cheung et al. [5] determined that the nucleate boiling frequency for downward-facing surfaces was lower than that of upward-facing surfaces due to differences in the boiling orientation. They also observed a 4 Hz vapor ejection frequency at the vessel's bottom center. Additionally, Gerardi et al. [20] found a nucleate boiling frequency of 11 Hz for an upward-facing surface undergoing pool boiling. Given Cheung's conclusion that the nucleate boiling frequency for a downward-facing surface would be less than that of an upward-facing surface (11 Hz), it is reasonable that a 7 Hz nucleate boiling frequency is observed in this experimental setup.

Using high-speed video and image processing, the interfacial oscillation frequency is determined by making use of a Windowed Fourier Transform (WFT). A window having 512 frames is chosen to carry out the WFT, which enables us to examine the dominant frequency for nearly every one second time instance (imaging

transformation and are obtained by fitting a circle to the detected edge for a fully-quenched hemisphere [28]. The measured film thickness from this high-speed video analysis has an accuracy of  $\pm 0.252$  mm, since the measurement resolution from the video data in the current setup is 0.252 mm/pixel. In the following section, quantitative insights demonstrate the physical significance of these results in relation to heat transfer and film boiling mechanisms.

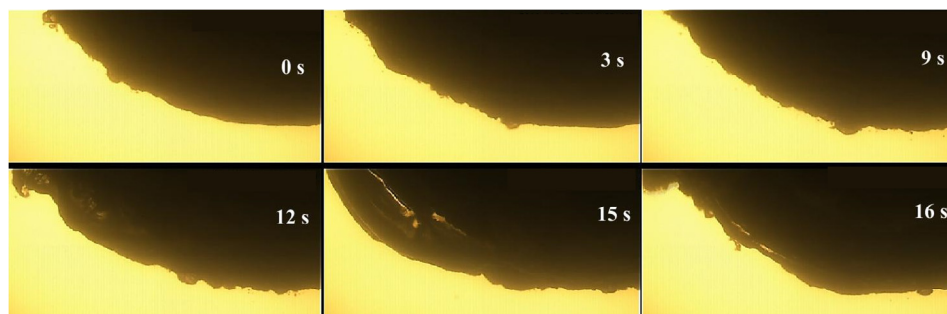


Fig. 2. Quenching process for the 100 °C bath at different moments in time.

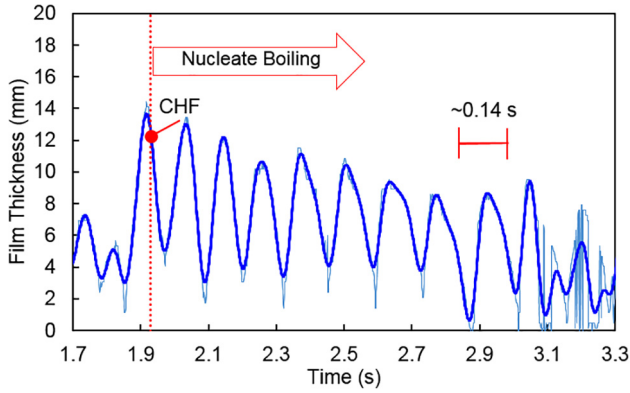


Fig. 4. Film thickness with time during nucleate boiling for the 90 °C bath.

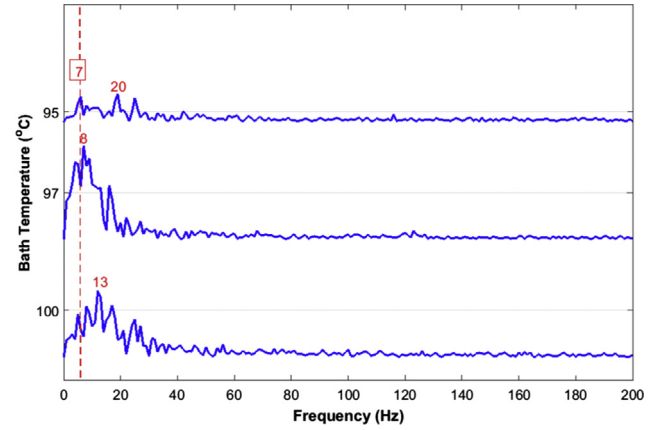


Fig. 5. Dominant frequencies for the 0° location at 0 s for three different bath temperatures of 95, 97, and 100 °C.

frequency is 650 Hz) [29]. Using a power spectral density (PSD) estimation [30], the progression of the interfacial oscillations is studied to determine the dominant frequency. In Fig. 5, the dominant frequencies are shown for three bath subcoolings with a PSD at 0 s after complete submersion of the vessel. Two characteristics can be noted in this figure, a high frequency peak and a high-frequency band. First, for each bath temperature of 95, 97, and 100 °C, there are associated dominant frequency peaks at 20, 8, and 13 Hz, respectively. Secondly, in addition to these dominant high frequency peaks, there is a high frequency band visible for all signals from approximately 8–30 Hz. These high frequencies are attributed to the fast interfacial oscillations in the vapor film. Additionally, there is another lower frequency peak that is detected in the 95 °C bath temperature: the 7 Hz frequency. This 7 Hz peak has been attributed to the vapor bulge frequency that resembles the nucleate boiling frequency in Fig. 4; the same frequency which was observed for the 90 °C bath after it achieves CHF. In Fig. 5, the 7 Hz peak is most visible in the 95 °C signal at 0 s of submersion. This 7 Hz peak is still noticeable for the 97 and 100 °C bath temperatures, but considerably decreases in intensity as the subcooling decreases. Since 7 Hz was observed as the nucleate boiling frequency from Fig. 4, and there is a noticeable peak at 7 Hz during film boiling for the 95 °C bath temperature, we can make the following statement: an artifact of the vapor bulge frequency is present in the signal. In other words, it can be said that the vapor bulge and nucleate boiling frequencies may not be independent since the end of film boiling dictates the beginning of nucleate boiling and this transition from one regime to another may induce some artifacts.

Since a lower bath temperature has a shorter transition from film to nucleate boiling, the progression of the 7 Hz nucleate boiling frequency is more visible for these experimental conditions. As observed in Fig. 5, an increase in bath subcooling intensifies the 7 Hz peak, suggesting that the vapor bulge frequency is embedded in the signal and becomes more dominant as quenching approaches. In other words, the embedded vapor bulge frequency, detected after the vessel has achieved CHF, has been identified and a precursor of this signal can be found during film boiling. Vapor bulges grow locally in the film when the interface moves closer to the hot surface. This movement enhances heat transfer by vaporizing the surrounding liquid and contributes to a vapor bulge similar to that of bubble nucleation on a vapor film [31].

In addition to comparing the dominant oscillation frequencies in the vapor film thickness with bath subcooling, PSDs have also been taken through time for all subcooled bath temperatures. In Fig. 6, however, only data for the 95 °C bath temperature is shown. Here, each signal is taken at one second intervals after vessel submersion for the first eight seconds of quenching. Similar to the

effect of bath subcooling, through time, the 7 Hz frequency intensifies during the quenching process. Again, this 7 Hz frequency has been attributed to the vapor bulge frequency, reiterating that as the vessel quenches and the temperature difference between the hot vessel wall and the bath temperature decreases, the 7 Hz oscillation becomes more dominant in the signal.

### 3.2. Film thickness study

In addition to calculating the film oscillation frequencies through time, film thicknesses were extracted for all subcoolings and compared with the corresponding vessel wall temperatures. Given that the thermocouple wire is 36-gauge and spot-welded to the inner vessel wall, the thermal time constant for such welds is approximately 0.1 s, corresponding to a maximum detectable frequency of 10 Hz [32,33]. Since 7 Hz is one of the dominant film oscillation frequencies and the thermocouple can detect up to 10 Hz, the effect of the vapor bulge can be accurately detected in the thermocouple signal. Given that the Biot number based on the wall thickness for the vessel is  $0.002 \ll 1$ , the local vessel wall temperature, as measured from the inside at 0.635 mm, is taken as the outer surface temperature. Vessel temperatures at the 0° angular location have been extracted and synchronized with the high-speed video. This effort provides insight into the evolution of film thickness with time and temperature. In Fig. 7, the film thickness at the 0° location is shown with respect to the vessel temperature for the 97 °C bath experiment. During film thickness measurement, the vessel temperature is well above the minimum film boiling temperature. Approximately 5 s after submersion, the film thickness drastically increases, varying between 1 and 2 mm initially and then climbing to 5 mm by approximately 14 s.

This rise in local film thickness is attributed to the unique quench progression of a downward-facing hemisphere. In Fig. 8 (a), a schematic diagram illustrates the quench progression of the vessel. Critical heat flux (CHF) occurs when liquid is able to contact the vessel wall, as can be seen from the photograph provided in Fig. 8(a). When CHF occurs at a particular location, large vapor bubbles form as contacting liquid rapidly evaporates, contributing to the vapor layer. The CHF is defined as the maximum heat flux determined by the transient thermocouple data in Eq. (1) as:

$$q''_{CHF} = \max \left( -C_p \rho_w x \frac{dT}{dt} \right), \quad (1)$$

where  $C_p$  is the specific heat of the vessel,  $\rho_w$  is the density of the vessel wall,  $x$  is the wall thickness, and  $\frac{dT}{dt}$  is the change in wall temperature with time. Once the upper angular locations begin to

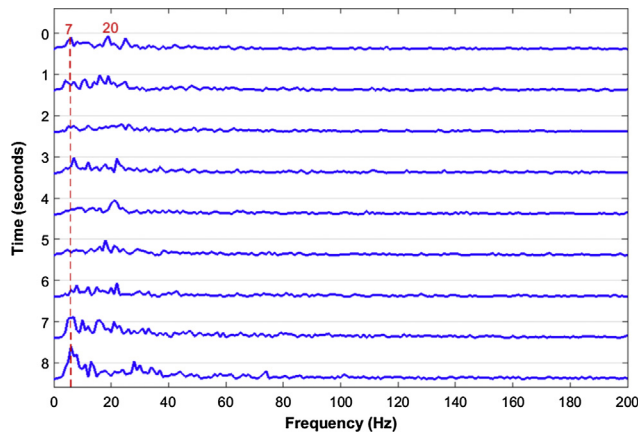


Fig. 6. Dominant frequencies through quench progression for the 95 °C bath.

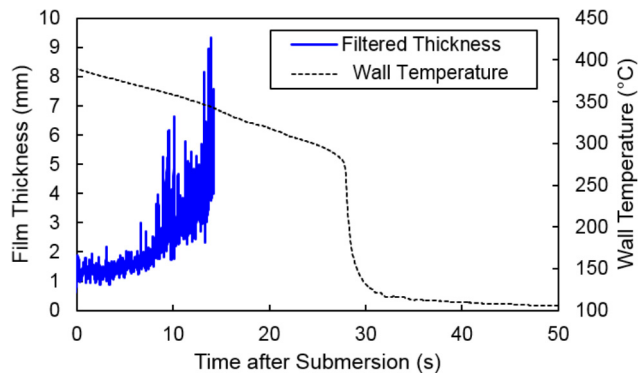


Fig. 7. Film thickness with vessel wall temperature for the 97 °C bath.

quench and the two-phase boundary layer becomes thicker at these locations, they act as a flow obstacle to the single-phase vapor film. The dynamics of angular locations upstream of the CHF, or quench location, are described as follows: from Fig. 8(a), as vapor is generated at the bottom center of the vessel, it begins to move upward through the continuous vapor film with a steady, increasing velocity until reaching the CHF location. At CHF, portions of the vessel are, or are in the process of becoming quenched. With intermediate liquid contacting the vessel wall, the single-phase vapor film merges with the two-phase boundary layer at the point of CHF. Now the vapor film cannot move with the same, steady velocity it previously had in the single-phase layer. This causes a large vapor bulge to form around the quench location, as seen in Fig. 8(a), which increases the local film thickness upstream. In film boiling when the wall temperature decreases, so does the heat flux; and when the film thickness increases, the heat flux will decrease. Considering these two phenomena, the increase in film thickness with time appears to be physically consistent. In Fig. 8(b), a time-line of three images, over the course of 0.06 s, shows the growth and movement of a vapor bulge up the side of the vessel.

In Fig. 9, film thickness with temperature is shown as a function of time for the 97 °C bath at the 0° angular location. Here, small “kinks” in the wall temperature correspond to abrupt increases in the film thickness. For example, one second after submersion, an increase in film thickness from 1.8 to 2.2 mm correlates to a small increase in the vessel wall temperature from 386.2 to 386.3 °C. Physically, as the vapor film becomes thicker, the insulating vapor blanket, which conducts heat poorly, will provide a local hot-spot for temperature rise. As the vapor film reaches a

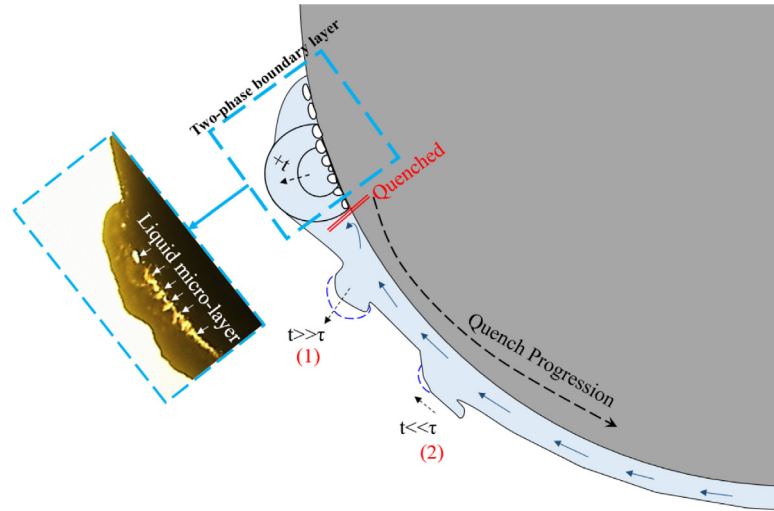
maximum thickness, a peak temperature is attained locally. When the vapor film thickness decreases, the conduction through the interface and the rate of heat transfer increase locally to produce a relative temperature “minimum.” A similar relationship between the local film thickness and relative instantaneous temperature has been observed at all subcoolings.

The film thickness at the 0° angular location is compared with different liquid bath temperatures in Fig. 10(a) and the variation in film thickness with angular location is compared in Fig. 10(b). In Fig. 10(a), the local film thickness at the 0° vessel bottom center is found to decrease with increasing liquid subcooling. There are two heat transfer mechanisms at work when the liquid bath is subcooled. First, part of the heat from the vessel wall is utilized to raise the liquid temperature, and the remaining heat is used for evaporation. Secondly, as the vapor film tries to grow outward, it is condensed by the subcooled bulk liquid [34–36]. For these two reasons, we observe a lower film thickness with increased subcooling. Comparing the effects of angular location on film thickness for a 95 °C bath, or 5 °C bath subcooling, Fig. 10(b) shows that as the angular location increases, so does the film thickness. Due to the violent nature of the quenching process, some low frequency vessel vibrations are noted for angles >14°. Since the vessel is fixed at the top of the support structure, the vibrations induce sideways oscillations with the fulcrum at the top of the support. In other words, the vessel may rotate about this location in a pendulum-like motion if there are any disturbances [28]. Regardless, the vapor film thickness will become larger at higher angular locations due to the effects of downstream quenching. Additionally, as the vessel produces vapor from the lower angular locations, that vapor travels up through the vapor film, growing in size by collecting vapor produced at all lower angles.

In Fig. 11, the variation of film thickness with angle and time is shown in the first second of submersion for the 95 °C bath temperature. Here, the color bar intensity represents the relative film thicknesses. Fig. 11(a) shows the vapor film on the hemispherical vessel, while Fig. 11(b) depicts a top-down view of the film thickness with time on a Cartesian plane. Since the image includes a portion of the vessel that is to the right of the vessel's bottom center, negative angles are depicted in Fig. 11(b), given the notation in Fig. 1(b). Fig. 11 demonstrates how the video data is converted into film thickness information, as part of the image processing that is performed. Note that the vapor film is thinner for lower angles and increases significantly for those angles above 21°.

### 3.3. Minimum and maximum film thicknesses at the vessel bottom center

While it has been established that the overall film thickness would increase with time (Fig. 8), the minimum and maximum film thicknesses can be extracted for all liquid subcoolings at the 0° angular location to demonstrate their time dependence. Fig. 12 shows the minimum and maximum film thicknesses for the 100 °C bath temperature, relative to time after vessel submersion. In Fig. 12, both the minimum and maximum film thicknesses increase with time as the vessel surface temperature decreases. For the time shown in the figure, vessel temperature remains well above the minimum film boiling temperature (275 °C), which is determined from thermocouple data. As discussed in Fig. 9, small jumps in the temperature correspond to local maxima in the film thickness, and temperature dips correspond to local film thickness minima. The average maximum, minimum, and overall average of both signals show an increase with time as the vessel quenches. The physical explanation for the increase in vapor film thickness with time lies in the downstream effects described in Fig. 8.



(a) Schematic diagram of film thickness progression with time after achieving CHF



(b) Progression of vapor bulge movement over 0.06 seconds

**Fig. 8.** Schematic depicting the physics of downward-facing quenching under pool boiling conditions.

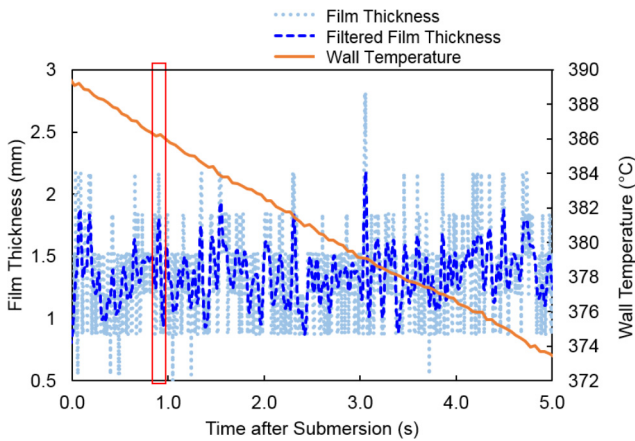


**Fig. 9.** Film thickness with vessel wall temperature for the 97 °C bath at the 0° angular location. Box highlights one such kink in film thickness corresponding to a local spike in vessel temperature.

### 3.4. Interfacial vapor bulge velocity

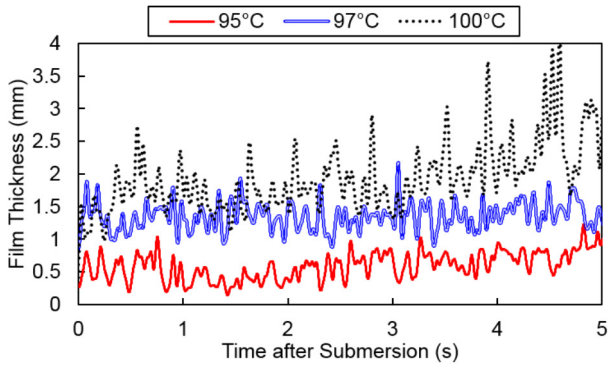
In addition to the vapor film thickness, Fig. 8(a) also shows the difference in vapor film dynamics between vapor bulge growth and movement. Let us consider two timescales associated with the vapor film. The first is the time it takes for the vapor bulge to grow outward, denoted by (1) in Fig. 8(a). The bubble growth time has been referred to as the vapor bulge frequency in Section 3.1 and from the frequency analysis, is determined to be 7 Hz. The second timescale is for the vapor bulge to migrate to higher angular locations, or what we will call “interfacial movement,” denoted by (2)

in Fig. 8(a). Here, the required time for a bubble to grow outward is much larger than the time required for a bubble to drift downstream to higher angular locations. In other words,  $\tau_{bubble\ growth} \gg \tau_{interfacial\ movement}$ . Given this observation, the interfacial velocities along the tangential direction have been determined using successive images sampled at each angular location. The interfacial velocity at different angular locations is shown in Fig. 13. To measure the interfacial velocity, two successive images are considered at one particular angular location. The pixel movement of an interface is taken for the two frames, and converted to a distance. With a known frequency of image acquisition, in this case 650 Hz, the interfacial velocity can be calculated. For each location, more than 90 sets of images were measured. Each represented velocity is the average of more than 30 data points, and the standard deviation is presented with error bars.

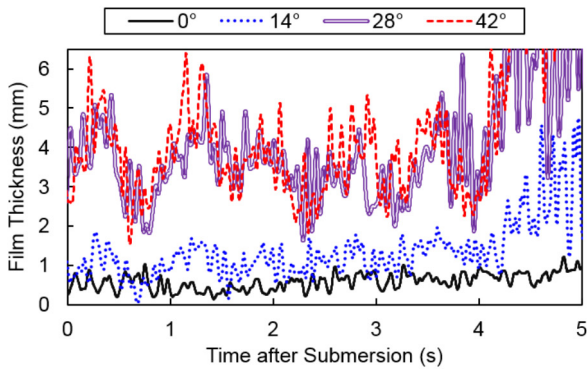
As shown in Fig. 13, the interfacial vapor velocities increase with an increase in the angular location. At the vessel bottom center, the velocity is close to zero, as some vapor will move either to the right or left side, averaging to approximately 0 m/s. At 14°, the vapor velocities are slightly higher, averaging around 0.15 m/s. However, from 14 to 28°, there is the largest jump in the vapor velocity, where the average velocity at 28° is approximately 1 m/s. At 42°, the average velocity seemingly stabilizes to 1.2 m/s. The present study does not show any prominent effect of liquid subcooling with the interfacial vapor velocity.

### 3.5. Interfacial heat transfer coefficient estimation

In order to estimate the heat flux at the vessel bottom center, the local heat transfer coefficient is required at this position. One key assumption for this analysis is that the interface at the bottom



(a) Film thickness with varied bath temperature at the 0° angular location



(b) Film thickness with varied angular locations for the 95°C bath

Fig. 10. Film thickness variation with bath temperature and angular location.

center is stationary, meaning that the interface is taken to be at a time-averaged or mean position. Given the control volume in Fig. 14, the region of interest is the liquid-vapor interface, where heat transfer occurs only in the normal direction to and from this location.

From conservation of mass on the control volume:

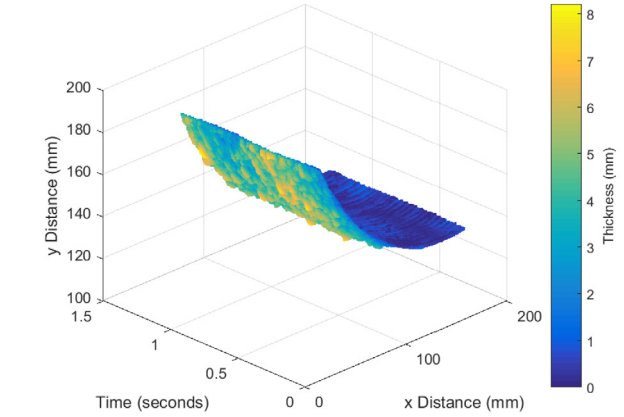
$$\rho_v V_v = \rho_l V_l, \quad (2)$$

where  $\rho$  is the density of liquid or vapor, and  $V$  is the velocity of these associated phases. In natural film boiling, the vapor film is not stationary; however, the interface will be treated as such when the vapor film is at an average film thickness. This assumption is accurate when the mass flow rate of vapor due to evaporation from the interface is equivalent to the mass flow rate of liquid coming towards the interface. In Fig. 14,  $q''_{cond,w-i}$  is the heat flux due to conduction from the wall to the interface,  $q''_{rad,w-i}$  is the heat flux due to radiation from the wall to the interface,  $q''_{SL,i-l}$  is the heat flux from the interface that provides sensible heating to the surrounding liquid, and  $q''_{evap,i-l}$  is the heat flux from the interface to the liquid which evaporates the surrounding liquid and contributes to the vapor film layer. Using the control volume established in Fig. 14, an energy balance at the interface yields:

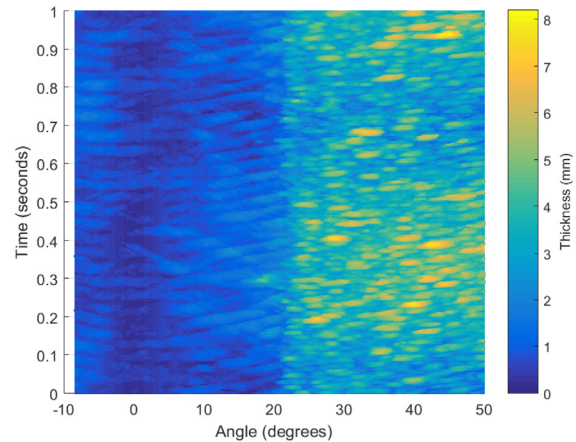
$$q''_{cond,w-i} + q''_{rad,w-i} - q''_{evap,i-l} - q''_{SL,i-l} = 0 \quad (3)$$

where,

$$q''_{cond,w-i} = \frac{k_v(T_W(t) - T_{SAT})}{\delta(t)} \quad (4)$$



(a) Isometric view of the variation in film thickness with position and time for 95°C bath temperature



(b) Top-down view of film thickness with angle and time for the 95°C bath temperature

Fig. 11. 3-D visualization of the vapor film thickness.

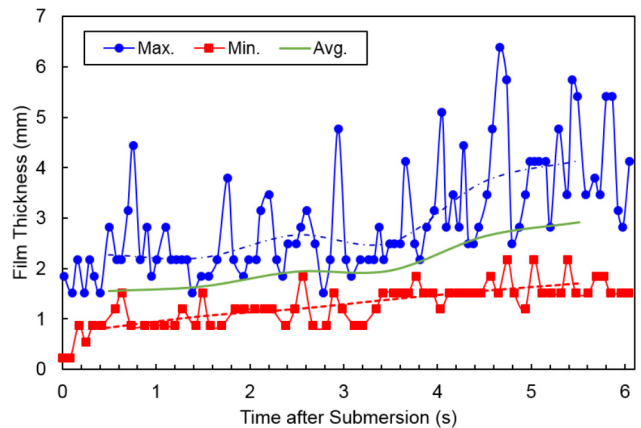


Fig. 12. Maximum, minimum, and average film thicknesses with time after vessel submersion for the 100 °C bath.

$$q''_{rad,w-i} = \frac{\sigma(T_W^4(t) - T_{SAT}^4)}{\frac{1}{\epsilon_W} + \frac{1}{\epsilon_L} - 1} \quad (5)$$

$$q''_{evap,i-l} = \rho_l V_l h_{lv} = m''_{evap} h_{lv} \quad (6)$$

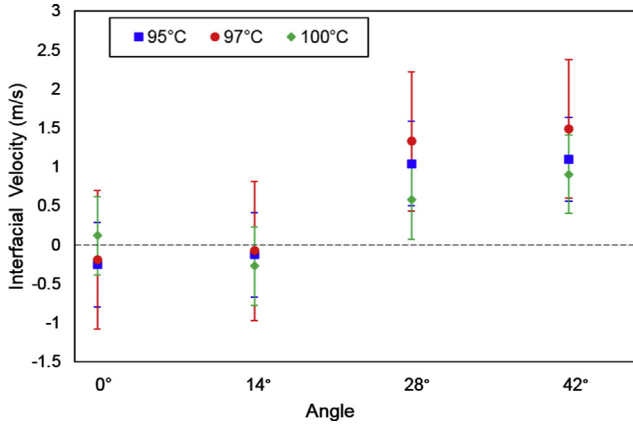


Fig. 13. Interfacial vapor film velocity with angle and bath temperature.

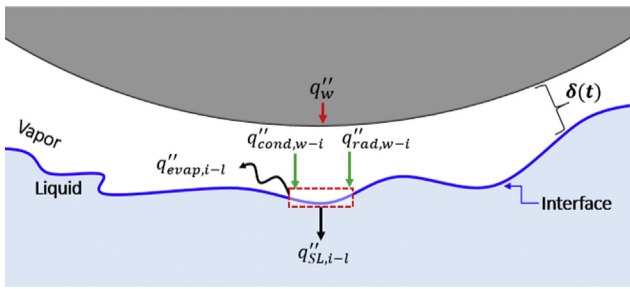


Fig. 14. Energy balance on the liquid-vapor interface at the vessel bottom center. The volume inside the dotted rectangle is the control volume.

$$q''_{SL,i-l} = h_{i-l}(T_{SAT} - T_L) \quad (7)$$

and  $k_v$  is the thermal conductivity of the vapor,  $\delta(t)$  is the vapor film thickness,  $T_W(t)$  is the transient wall temperature,  $T_L$  is the liquid bath temperature,  $T_{SAT}$  is the saturation temperature at atmospheric pressure,  $\sigma$  is the Stefan-Boltzmann constant,  $\epsilon_W$  and  $\epsilon_L$  are the emissivities of the wall and liquid, respectively,  $m''_{evap}$  is the mass flux due to evaporation, and  $h_{lv}$  is the latent heat of vaporization.

To determine the heat flux due to the sensible heating of liquid ( $q''_{SL,i-l}$ ), the heat transfer coefficient from the interface to the bulk liquid,  $h_{i-l}$  must be known. Since the interfacial heat transfer coefficient fluctuates with the film thickness throughout the quenching process, it is difficult to model its value. However, when the film thickness is maximum at the vessel bottom center, the interfacial velocity, equivalent to the change in film thickness with time, will be zero as seen in Eq. (8):

$$V_l = \left. \frac{d\delta}{dt} \right|_{\delta=\delta_{avg}} \quad (8)$$

In Eq. (8),  $V_l$  is the liquid velocity at the interface, derived from the measured film thickness ( $\delta(t)$ ) that has been extracted during stable film boiling for the time durations shown in Fig. 15. The interfacial velocity will be zero when the film thickness is maximum because there will be no additional vapor growth or evaporation at that time. At maximum film thickness,  $q''_{evap,i-l}$  will also be zero from Eqs. (6), and (3) simplifies to:

$$q''_{cond,w-i} + q''_{rad,w-i} = q''_{SL,i-l} \quad (9)$$

Substituting the values for the heat fluxes (Eqs. (4), (5) and (7)) into Eq. (9), yields a solution for the interfacial heat transfer coefficient  $h_{i-l}$  that can now be written in terms of known quantities when the vapor film thickness is at a maximum:

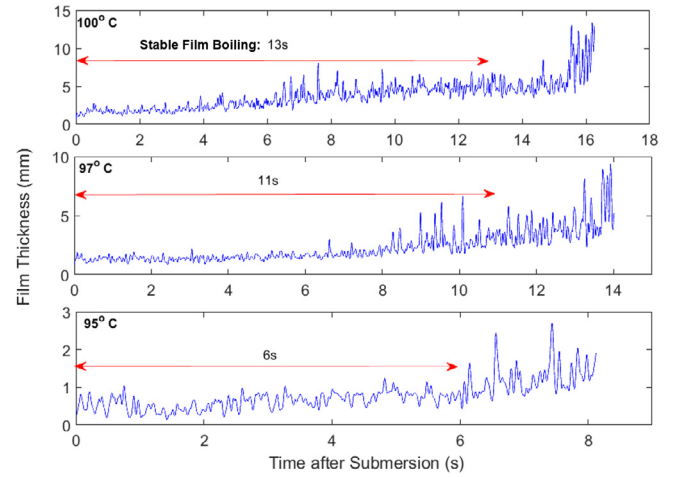


Fig. 15. Regions of stable film boiling for each bath temperature.

$$h_{i-l}(t) = \frac{k_v}{\delta_{MAX}(t)} \frac{T_W(t) - T_{SAT}}{T_{SAT} - T_L} + \frac{\sigma(T_W^4(t) - T_{SAT}^4)}{\left(\frac{1}{\epsilon_W} + \frac{1}{\epsilon_L} - 1\right)(T_{SAT} - T_L)} \quad (10)$$

The calculated heat transfer coefficient at the interface (Eq. (10)), is compared with the correlation for the interfacial heat transfer given by Kelly (Eq. (11)) for inverted annular flow boiling on a heated rod [37]. While Kelly's correlation is for a vertical rod, it is the only correlation available in the literature for interfacial heat transfer, and as such, the two heat transfer coefficients are shown for comparison. Kelly's correlation follows as:

$$h_{Kelly,2015}(t) = \frac{130}{\delta_{avg}(t)} (C_{p,L} \mu_L k_L)^{1/2}, \quad (11)$$

where  $C_{p,L}$ ,  $\mu_L$ , and  $k_L$  are the specific heat, viscosity, and thermal conductivity of the liquid phase, respectively.

The modal values for the heat transfer coefficients are compared at three different liquid bath temperatures shown in Fig. 16. From the figure, the heat transfer coefficients were calculated in the regions of stable film boiling (see Fig. 15), and their frequencies, at different magnitudes, show the probability of a particular coefficient value under the respective conditions. To model Eq. (10), the maximum film thickness,  $\delta_{MAX}$ , is extracted every 5 Hz (0.2 s) to determine its value in that interval. Then, that maximum film thickness is used to solve for  $h_{i-l}(t)$  every 5 Hz. In contrast, Kelly's Eq. (11) is modeled using an average film thickness extracted at 5 Hz intervals to determine  $\delta_{avg}(t)$ . As the bath temperature increases, the heat transfer coefficients appear to decrease, with  $h_{Kelly,2015}$  predicting larger values than  $h_{i-l}(t)$ .

While the two methods provide coefficients of the same order of magnitude, the values of  $h_{i-l}(t)$  were selected for the following analyses due to the differences in geometry for Kelly's model, Eq. (11). The modal value of  $h_{i-l}(t)$ , in the period of stable film boiling, is used to define  $q''_{SL,i-l}$  and ultimately the total heat flux balance derived in the following section.

### 3.6. Heat flux comparison using video data

The following section provides an alternative method to calculating the heat flux on the vessel bottom center by utilizing the vapor film thickness measured from the high-speed video data. Two methods are used to estimate the heat flux; the first method uses a traditional lumped capacitance (L-C) formulation and the second proposed method utilizes both thermocouple and video data (T-V) to compare the results. Derived from a transient energy

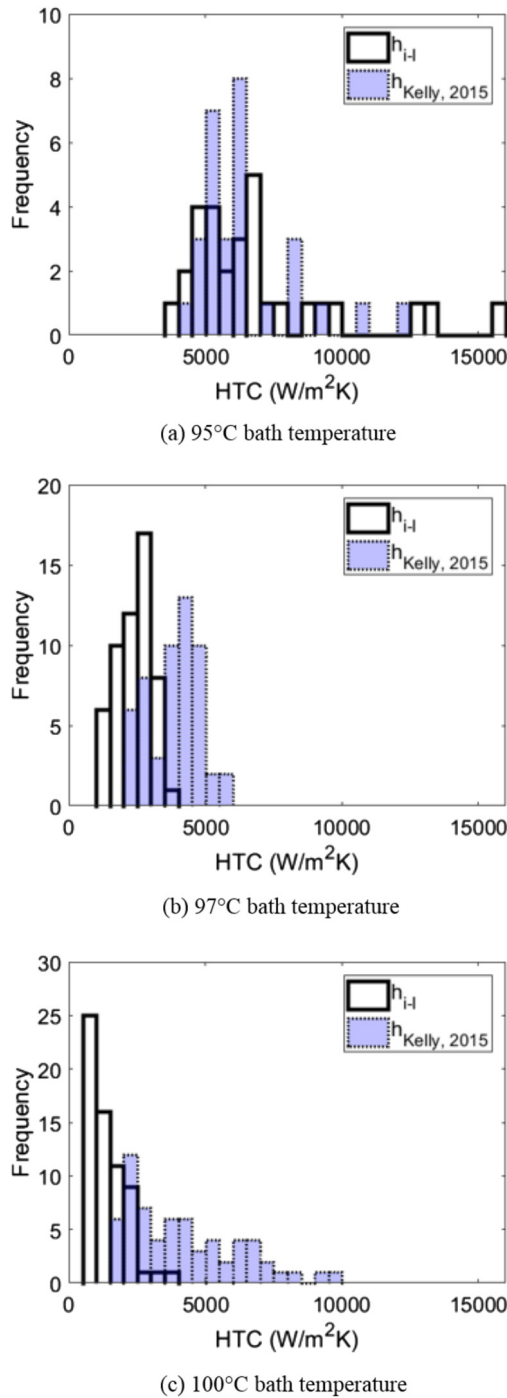


Fig. 16. Heat transfer coefficients (HTCs) for different bath temperatures.

balance on the vessel wall, the heat flux obtained from the (L-C) method is defined as:

$$q''_{L-C} = -C_p \rho_w x \frac{dT}{dt}, \quad (12)$$

which is the heat flux into the control volume as determined by thermocouple data. Here,  $C_p$  is the specific heat of the vessel,  $\rho_w$  is the density of the vessel, and  $x$  is the vessel wall thickness.

Additionally, the heat flux determined by the (T-V) method follows as:

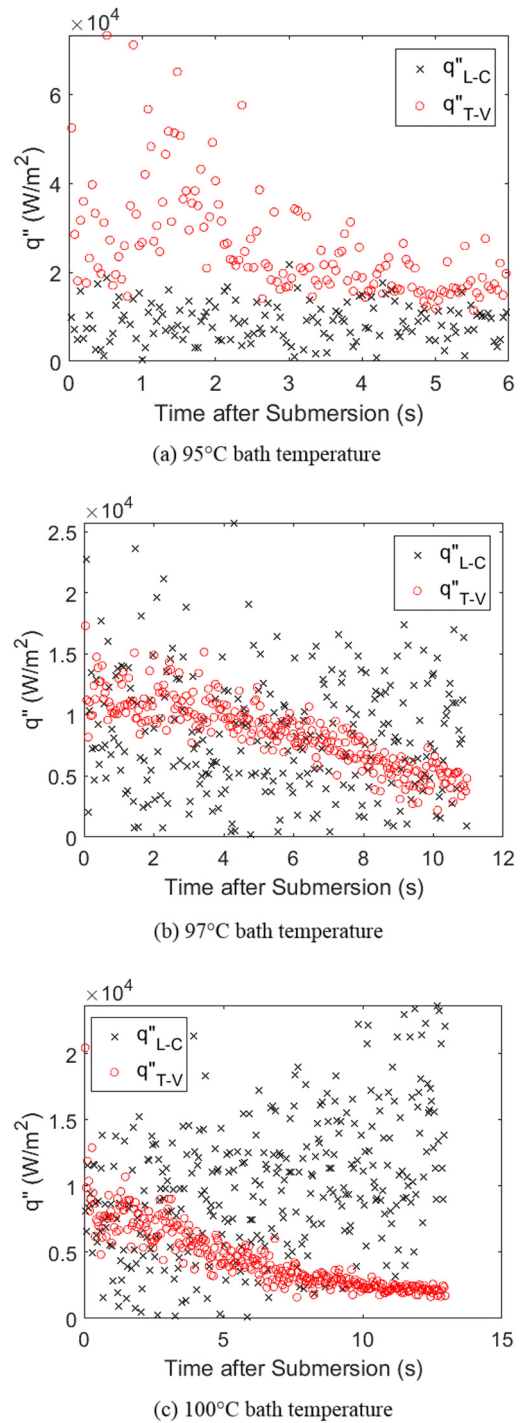


Fig. 17. Heat fluxes calculated by lumped capacitance (L-C) and thermocouple-video (T-V) methods.

$$q''_{T-V} = q''_{cond,w-i} + q''_{rad,w-i} = \frac{k_v(T_W(t) - T_{SAT})}{\delta(t)} + \frac{\sigma(T_W^4(t) - T_{SAT}^4)}{\left(\frac{1}{\epsilon_w} + \frac{1}{\epsilon_L} - 1\right)}. \quad (13)$$

The heat flux at the interface in Eq. (13) is calculated by fusing information obtained from both thermocouple and video data. We estimate the film thickness from the extracted video data and measure  $T_W(t)$  from the thermocouples embedded in the vessel wall.

Both  $q''_{L-C}$  and  $q''_{T-V}$ , Eqs. (12) and (13) respectively, are used to determine the heat fluxes in Fig. 17 for the different liquid bath temperatures. For the 95 °C bath, shown in Fig. 17(a),  $q''_{L-C}$  is significantly less than that of  $q''_{T-V}$ . However, as the bath temperature increases in Fig. 17(b) and (c), the values for  $q''_{L-C}$  increase with time. Additionally,  $q''_{L-C}$  has a much larger spread when compared with  $q''_{T-V}$ . In fact, as the bath temperature increases from 95 to 97 and 100 °C,  $q''_{L-C}$  increases with the time, whereas,  $q''_{T-V}$  decreases with time after vessel submersion.

The differences in behavior between  $q''_{L-C}$  and  $q''_{T-V}$  with time and bath temperature originate from their definitions and associated assumptions. For  $q''_{L-C}$ , the heat flux from the wall depends on the change in the temperature response with time. Since the vessel temperature decreases steadily in the film boiling regime, the temperature change will be large and positive, increasing with time after vessel submersion. However, for  $q''_{T-V}$  the heat flux from the wall is inversely proportional to the film thickness, which increases with time (see discussion of Fig. 8(a)).

In addition to the differences in formulation, distinctions between the two heat flux methods may be due to the assumptions made for  $q''_{T-V}$ , which include: (1) the energy loss due to advection through the vapor film is negligible, and (2)  $V_l$  can be represented by a time averaged film thickness in Eq. (8). Both assumptions may have contributed to the underestimation of  $q''_{T-V}$  when compared with  $q''_{L-C}$ . Further investigation concerning the differences between the two heat flux methods is required in future work.

By comparing these methods for the heat flux, the feasibility to estimate this value through the use of multiple sensors has been established. While not equivalent, both methods produce results of comparable magnitude that can be explained based on their differences in methodology and formulation.

#### 4. Conclusions

The following important aspects of the research conducted in this article are summarized below:

1. An image processing technique utilizing thresholding and edge detection is useful for extracting the interfacial vapor film thickness through time. Thermocouple sensors synchronized with high-speed video can provide useful insight into the thermal-hydraulic behavior of interfacial vapor films during pool boiling of a downward-facing hemisphere.
2. With this measurement technique, quantitative observations using visual sensors can be made, which were not otherwise apparent. These observations include: interfacial oscillation frequency with time, film thickness behavior with vessel wall temperature, film thickness response to liquid subcooling, and interfacial velocity behavior with vessel angular location.
3. The interfacial heat transfer coefficient has been determined for the 0° angular location during film boiling for different bath temperatures. Additionally, these values are comparable with results obtained from Kelly's correlation [37] for film boiling on a rod geometry.
4. The heat flux at the vessel bottom center has been calculated using two different methods; a traditional lumped capacitance and a new method that utilizes thermocouple and film thickness measurements from the video data. The proposed method for determining the heat flux is presented as an additional technique, utilizing video and thermocouple information, to model its values in the film boiling regime.

#### Conflict of interest

None.

#### Acknowledgments

The lead author would like to acknowledge the Kevin L. Wert Memorial Scholarship for supporting this work. The late Dr. Kevin L. Wert was a gifted scientist in the field of two-phase heat transfer and his contributions to the literature have greatly furthered research in this area.

#### Appendix A. Supplementary material

Supplementary data associated with this article can be found, in the online version, at <https://doi.org/10.1016/j.ijheatmasstransfer.2018.04.091>.

#### References

- [1] S. Rouge, Sultan test facility for large-scale vessel coolability in natural convection at low pressure, *Nucl. Eng. Des.* 169 (1–3) (1997) 185–195.
- [2] S. Rouge, I. Dor, G. Geffraye, Reactor vessel external cooling for corium retention sultan experimental program and modelling with CATHARE code, Tech. rep., 1999.
- [3] T. Chu, B. Bainbridge, R. Simpson, J. Bentz, Ex-vessel boiling experiments: laboratory-and reactor-scale testing of the flooded cavity concept for in-vessel core retention part I: observation of quenching of downward-facing surfaces, *Nucl. Eng. Des.* 169 (1–3) (1997) 77–88.
- [4] M.J. Brusstar, H. Merte, R.B. Keller, B.J. Kirby, Effects of heater surface orientation on the critical heat flux-I. An experimental evaluation of models for subcooled pool boiling, *Int. J. Heat Mass Transf.* 40 (17) (1997) 4007–4019.
- [5] F.-B. Cheung, K.H. Haddad, Y. Liu, Critical heat flux (CHF) phenomenon on a downward facing curved surface, Tech. rep., Nuclear Regulatory Commission, Washington, DC (United States). Div. of Systems Technology; Pennsylvania State Univ., University Park, PA (United States). Dept. of Mechanical Engineering, 1997.
- [6] F.-B. Cheung, K. Haddad, A hydrodynamic critical heat flux model for saturated pool boiling on a downward facing curved heating surface, *Int. J. Heat Mass Transf.* 40 (6) (1997) 1291–1302.
- [7] F.-B. Cheung, J. Yang, M. Dizon, J. Rempe, K. Suh, S. Kim, P. Ragesh, K. Sreenivas, S. Dasgupta, S. De, et al., Scaling of downward facing boiling and steam venting in a heated hemispherical annular channel, *Int. J. Transp. Phenom.* 6 (2004) 147–162.
- [8] F.-B. Cheung, J. Yang, M. Dizon, J. Rempe, K. Suh, S. Kim, On the enhancement of external reactor vessel cooling of high-power reactors, 2003.
- [9] F.A. Sohag, F.R. Beck, L. Mohanta, F.-B. Cheung, A.E. Segall, T.J. Eden, J.K. Potter, Effects of subcooling on downward facing boiling heat transfer with micro-porous coating formed by cold spray technique, *Int. J. Heat Mass Transf.* 106 (2017) 767–780.
- [10] F.A. Sohag, F.R. Beck, L. Mohanta, F.-B. Cheung, A.E. Segall, T.J. Eden, J.K. Potter, Enhancement of downward-facing saturated boiling heat transfer by the cold spray technique, *Nucl. Eng. Technol.* 49 (1) (2017) 113–122.
- [11] F.A. Sohag, On the enhancement of downward facing boiling heat transfer using micro-porous coating (Ph.D. thesis), Pennsylvania State University, 2016.
- [12] A.E. Segall, F.A. Sohag, F.R. Beck, L. Mohanta, F.-B. Cheung, T.J. Eden, J. Potter, Microporous coatings and enhanced critical heat flux for downward facing boiling during passive emergency reactor cooling, *J. Pressure Vessel Technol.* 139 (5) (2017) 051601.
- [13] S.H. Pham, Z. Kawara, T. Yokomine, T. Kunugi, Detailed observations of wavy interface behaviors of annular two-phase flow on rod bundle geometry, *Int. J. Multiph. Flow* 59 (2014) 135–144.
- [14] S.H. Pham, Z. Kawara, T. Yokomine, T. Kunugi, Measurements of liquid film and droplets of annular two-phase flow on a rod-bundle geometry with spacer, *Int. J. Multiph. Flow* 70 (2015) 35–57.
- [15] C.S. Brooks, T. Hibiki, Wall nucleation modeling in subcooled boiling flow, *Int. J. Heat Mass Transf.* 86 (2015) 183–196.
- [16] Y.S. Chang, K.-H. Jeong, H.J. Lee, Y.P. Lee, H.-Y. Kim, Behavior of thermal bubbles formed from a single nucleation site, *J. Mech. Sci. Technol.* 24 (1) (2010) 415–420.
- [17] X. Fu, P. Zhang, C. Huang, R. Wang, Bubble growth, departure and the following flow pattern evolution during flow boiling in a mini-tube, *Int. J. Heat Mass Transf.* 53 (21) (2010) 4819–4831.
- [18] D.J. Rodriguez, T.A. Shedd, Entrainment of gas in the liquid film of horizontal, annular, two-phase flow, *Int. J. Multiph. Flow* 30 (6) (2004) 565–583.
- [19] I. Zadrzail, O.K. Matar, C.N. Markides, An experimental characterization of downwards gas-liquid annular flow by laser-induced fluorescence: flow regimes and film statistics, *Int. J. Multiph. Flow* 60 (2014) 87–102.

- [20] C. Gerardi, J. Buongiorno, L.-W. Hu, T. McKrell, Study of bubble growth in water pool boiling through synchronized, infrared thermometry and high-speed video, *Int. J. Heat Mass Transf.* 53 (19) (2010) 4185–4192.
- [21] C.-J. Kuo, A. Koar, Y. Peles, S. Virost, C. Mishra, M.K. Jensen, Bubble dynamics during boiling in enhanced surface microchannels, *J. Microelectromech. Syst.* 15 (6) (2006) 1514–1527.
- [22] S. Hamzekhani, M.M. Falahieh, M.R. Kamalizadeh, Z. Nazari, Experimental study on bubble departure frequency for pool boiling of water/NaCl solutions, *Heat Mass Transf.* 51 (9) (2015) 1313–1320.
- [23] G. Hazi, A. Markus, On the bubble departure diameter and release frequency based on numerical simulation results, *Int. J. Heat Mass Transf.* 52 (5) (2009) 1472–1480.
- [24] I. Malenkov, The frequency of vapor-bubble separation as a function of bubble size, *Fluid Mech. Sov. Res.* 1 (36–42) (1972) 143.
- [25] J. Kim, M.H. Kim, On the departure behaviors of bubble at nucleate pool boiling, *Int. J. Multiph. Flow* 32 (10) (2006) 1269–1286.
- [26] D.E. Kim, D.I. Yu, S.C. Park, H.J. Kwak, H.S. Ahn, Critical heat flux triggering mechanism on micro-structured surfaces: coalesced bubble departure frequency and liquid furnishing capability, *Int. J. Heat Mass Transf.* 91 (2015) 1237–1247.
- [27] D. Marr, E. Hildreth, Theory of edge detection, *Proc. R. Soc. Lond. B.* 207 (1167) (1980) 187–217.
- [28] C.-S. Jao, F.R. Beck, N. Virani, F.-B. Cheung, A. Ray, Analysis of filtered thermal-fluid video data from downward facing boiling experiments, *J. Dyn. Syst. Meas. Contr.* 140 (7) (2018) 074502.
- [29] S.A. Fulop, K. Fitz, Algorithms for computing the time-corrected instantaneous frequency (reassigned) spectrogram, with applications, *J. Acoust. Soc. Am.* 119 (1) (2006) 360–371.
- [30] M.P. Norton, D.G. Karczub, *Fundamentals of Noise and Vibration Analysis for Engineers*, Cambridge University Press, 2003.
- [31] T. Bui, V. Dhir, Film boiling heat transfer on an isothermal vertical surface, *J. Heat Transf.* 107 (4) (1985) 764–771.
- [32] S.T. Francis, I.E. Morse, *Measurement and Instrumentation in Engineering: Principles and Basic Laboratory Experiments*, vol. 67, CRC Press, 1989.
- [33] Omega Engineering: Thermocouple Response Time. <<http://www.omega.com/techref/ThermocoupleResponseTime.html>> (accessed: 2017-07-30).
- [34] L. Mohanta, F.-B. Cheung, S.M. Bajorek, Stability of coaxial jets confined in a tube with heat and mass transfer, *Physica A* 443 (2016) 333–346.
- [35] L. Mohanta, *Theoretical and Experimental Study of Inverted Annular Film Boiling and Regime Transition During Reflood Transients*, The Pennsylvania State University, 2015.
- [36] L. Mohanta, F.A. Sohag, F.-B. Cheung, S.M. Bajorek, J.M. Kelly, K. Tien, C.L. Hoxie, Heat transfer correlation for film boiling in vertical upward flow, *Int. J. Heat Mass Transf.* 107 (2017) 112–122.
- [37] J. Kelly, Liquid-side interfacial heat transfer in inverted annular film boiling, in: *Conference Proceedings of NURETH-16*, Chicago, IL, August 30–September 4, 2015, 2015, pp. 6849–6862.